Tuning Adsorption-Induced Responsiveness of a Flexible Metal–Organic Framework JUK-8 by Linker Halogenation

Kornel Roztocki, Filip Formalik, Volodymyr Bon, Anna Krawczuk, Piotr Goszczycki, Bogdan Kuchta, Stefan Kaskel, Dariusz Matoga

CHEMISTRY OF MATERIALS

pubs.acs.org/cm

Article

Tuning Adsorption-Induced Responsiveness of a Flexible Metal–Organic Framework JUK-8 by Linker Halogenation

Kornel Roztocki,* Filip Formalik, Volodymyr Bon, Anna Krawczuk, Piotr Goszczycki, Bogdan Kuchta, Stefan Kaskel, and Dariusz Matoga*

Cite This: https://doi.org/10.1021/acs.chemmater.2c00249

Read Online

ACCESS | Metrics & More | Article Recommendations | Supporting Information

ABSTRACT: Flexible stimuli-responsive metal–organic frameworks have become promising candidates for numerous applications in gas-related technologies; however, the methods of fine tuning their responses are still limited and sought after. In this work, we demonstrate control over the adsorption properties of a flexible platform by incorporating halogen substituents (X = F, Cl, Br, I) into an eightfold interpenetrated isoreticular series $[Zn(oba)(X\text{-}pip)]_n$ (**JUK-8X**; *X-pip* = 4-pyridyl-functionalized benzene-1,3-dicarbo-5-halogenohydrazide; oba^{2-} = 4,4′-oxydibenzoic carboxylate). The introduced halogen atoms allow for precise tuning of CO_2 gate-opening pressures from p/p_0 = 0.08 for the parental **JUK-8** to 0.78 for the chlorine-functionalized **JUK-8Cl**. The presence of fluorine or chlorine substituent in the X-pip linker practically does not influence the maximum molar CO_2 uptake as compared to **JUK-8**, whereas larger bromine or iodine atoms increase this uptake by 59 and 48%, respectively. Utilizing in situ powder X-ray diffraction (PXRD) during CO_2 adsorption for a model **JUK-8F**, we propose a detailed mechanism of phase transitions including positions of the adsorbed gas molecules for the two loaded phases. Density functional theory calculations supported by in situ PXRD measurements at a saturation pressure shed light on the unusual CO_2 adsorption properties of **JUK-8Br** and **JUK-8I**. Overall, our report demonstrates the use of halogen interactions for the control of a gas-responsive system and provides insightful guidance for the further development of flexible, adaptable materials.

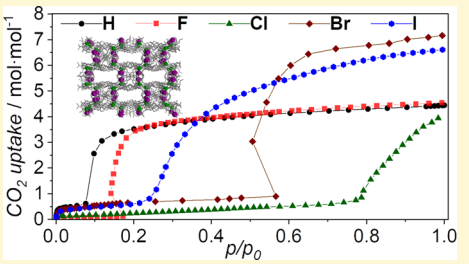

1. INTRODUCTION

Crystalline metal–organic frameworks (MOFs), which are built of metallic nodes and organic linkers, have either rigid[1−3] or flexible[4−6] porous structures. Due to their unique properties, not observed in other porous materials,[7−9] the flexible MOFs have attracted increasing scientific attention for the last two decades[10−18] as materials with a predicted large impact on gas-related technologies.[19−23] Majority of flexible MOFs undergo transition to nonporous or less porous phases upon temperature- or pressure-induced desolvation, whereas gas adsorption reverses these processes,[10−12] and at a specific pressure, which exceeds an energetic barrier, crystal structures of flexible MOFs transform to open phases. Apart from a few exceptions, such as SHF-61,[24] the observed phase transitions occur between energetic minima, and the cell volume during adsorption changes abruptly, which manifests itself as one or a few distinguishable steps in an isotherm plot. In a desorption branch, the opposite phenomena occur, and a reversal of the cell volume changes pushes adsorbate molecules out of the pores. If this return occurs directly from porous to nonporous phases, it gives a considerable advantage to such flexible MOFs for pressure swing gas-storage applications in comparison to rigid materials.[23,25] Here, one of the most important goals, apart from assuring cyclability, is a precise control over pressure steps during gas uptake and release. It has been achieved only in a few systems so far. Long and co-workers[26] have tuned the adsorption-induced phase transition of Co(X-bdp) (bdp^{2-} = 1,4-benzenedipyrazolate; X = F, p-F_2, o-F_2, D_4, p-Me; where p = para and o = ortho positions) by an edge-to-face $\pi\cdots\pi$ interaction. These phenomena were analyzed by powder X-ray diffraction (PXRD) experiments for desolvated phases and in situ studies during adsorption. Zaworotko et al. employed different N-donor linkers for controlling the gate-opening pressure in a series of MOFs with the *pcu* topology.[27] Other promising methods included changing the composition of metal nodes,[28] linker modification,[29−32] crystal size engineering,[33] changing sample pretreatment,[34] or adjusting the solvents used in the synthesis.[35] Nonetheless, the reports that simultaneously describe control over properties of flexible MOFs with real-time mechanistic insights into stimuli-responsiveness are still very rare and far between.[26,29,32] Further progress in the field may be achieved by incorporating underexplored weak interactions (e.g., involving halogens[36−39]) into flexible platforms, combined with a holistic

Received: January 26, 2022
Revised: March 18, 2022

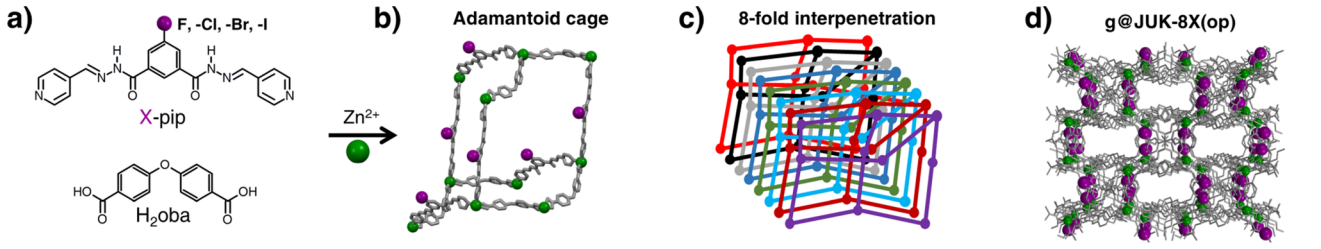

Figure 1. Synthetic route and structural features of the **g@JUK-8X(op)** series: (a) Structural formulas of linker precursors used in the synthesis: 4-pyridyl-functionalized benzene-1,3-dicarbo-5-halogenohydrazide (*X-pip*) and 4,4′-oxybis(benzenedicarboxylic acid) (H_2*oba*). (b) Adamantoid cage in a single dia network. (c) Eightfold interpenetration of dia networks. (d) Entrance to 1D channels; view along the *c* direction.

understanding of their impact on stimuli-responsiveness enabled by both ex and in situ techniques.

In this work, we have incorporated a series of halogen substituents (F, Cl, Br, and I) into a model **JUK-8** platform (Jagiellonian University in Kraków, material no. 8) and holistically investigated the influence of additional interactions on its adsorption properties including gate-opening pressure and maximum uptake of CO_2 at 195 K. **JUK-8** is a mixed-linker eightfold interpenetrated water-stable member[40] of an acylhydrazone-based family of MOFs.[41] These materials contain dual-type functional groups which may serve as donors and acceptors in hydrogen bonding, and hence they may display properties similar to those of biological systems, for example, structural transformations depending on subtle hydrogen bond networks[40,42,43] or catalytic activity.[44] Our studies show that an additional fluorine or chlorine atom attached to a central ring of an N-donor linker in **JUK-8X** nearly does not influence a maximum molar CO_2 uptake compared to the parental isostructural framework **JUK-8**, yet these halogens change the mechanism of adsorption. Counter-intuitively, larger bromine or iodine atoms considerably increase CO_2 loading at a saturation pressure. By utilizing in situ PXRD during carbon dioxide adsorption (at 195 K) and computational simulations, we provide in-depth insights into the behavior of the isoreticular **JUK-8X** series. Overall, our report demonstrates the use of halogen interactions for the control of a gas-responsive system and provides insightful guidance for the further development of such materials.

2. RESULTS AND DISCUSSION

2.1. Synthesis of Functionalized JUK-8 Derivatives. In order to investigate the influence of halogen substituents on the stimuli-responsiveness of the **JUK-8** platform, a series of new linkers, 4-pyridyl-functionalized benzene-1,3-dicarbo-5-halogenohydrazides (*X-pip*; X = F, Cl, Br, or I) was prepared in the reaction between appropriate 5-X-isopthalic hydrazide and 4-pyridinecarboxaldehyde in the presence of trichloroacetic acid as a catalyst (Scheme S1, Supporting Information). A 2-day long heating of *X-pip* ligand, 4,4′-oxydibenzoic acid (H_2*oba*), with zinc(II) nitrate in DMF/water solution yielded four new humidity-stable microporous MOFs $\{[Zn(oba)(X\text{-}pip)]\cdot 3H_2O\cdot 2DMF\}_n$ (**JUK-8X**; Figures 1 and S1, Supporting Information). After optimizing the reaction conditions, single crystals of fluorine and iodine derivatives suitable for single-crystal X-ray diffraction (SC-XRD) analysis were prepared in a small scale, whereas crystals of **JUK-8Cl** and **JUK-8Br** were selected from the bulk (see the Supporting Information for details). The as-synthesized compounds, stable at ambient conditions, are denoted as **g@JUK-8X(op)** to indicate their open-pore (**op**) phases (g denotes guest molecules = $3H_2O$ and 2DMF).

Crystal structures of **g@JUK-8X(op)**, determined from SC-XRD measurements, reveal that the obtained materials crystalize as twins in the monoclinic space group (*Cc*) and consist of eightfold interpenetrated networks of *dia* topology, each containing adamantoid cages with Zn···Zn edges of 14.3−14.7 and 22.8−23.0 Å in length (Tables S1 and S2, Supporting Information). Despite a high level of interpenetration, the materials possess one-dimensional (1D) channels propagating along the *c* direction (Figures 1 and S2, Supporting Information). As expected, the halogen-functionalized family is isostructural to the previously published **JUK-8** compound;[40] however, the increasing substituent radius (from H to I) causes swelling of the unit cell (the unit cell volume increases from 8050 to 8559 Å^3) and influences the geometry of the pores (Table S1 and Figures S2 and S3, Supporting Information). The detailed computational structural analysis[45] reveals that **g@JUK-8I(op)** and **g@JUK-8Br(op)** possess two nonequivalent types of coordination centers: Zn1 with a deformed octahedral and Zn2 with a deformed trigonal bipyramidal geometries. Thus, eightfold interpenetrated networks show [4 + 4] configuration (Figure S4, Supporting Information). A similar effect is observed for the other as-synthesized halogen derivatives of **JUK-8**, however, without the influence on the coordination number of the zinc ion.

Analogically to the parent **JUK-8** structure, the interpenetrating networks of **g@JUK-8X(op)** are connected via $\pi\cdots\pi$ interactions and $(N-H)_{pip}\cdots O_{oba}$ hydrogen bonds between acylhydrazone and carboxylate groups (Figure S5 and Table S3, Supporting Information). However, the introduction of halogen atoms gives rise to additional nonbonding contacts between two adjacent *X-pip* linkers. The distance between a halogen substituent in the central *X-pip* ring and the oxygen atom of the acylhydrazone carbonyl group is smaller than the sum of their van der Waals[46] radii and indicates the presence of weak halogen-oxygen[37] interactions: *d*(CO···XC) = 3.173, 3.323, and 3.330 Å for Cl, Br, and I, respectively (Figure S5, Supporting Information). Furthermore, the high electronegativity of fluorine is responsible for the appearance of an extra interaction between the oxygen atom of the acylhydrazone group and the carbon atom of the *F-pip* central ring: *d*(O···CF) = 3.195 Å.

2.2. Structural Characterization of Closed-Pore Phases. Thermogravimetric analysis and variable temperature PXRD (VT-PXRD) experiments reveal that the heated **g@JUK-8X(op)** release guest molecules at approximately 140−170 °C (Figures S6 and S7, Supporting Information). This thermal stimulus induces a transition of the as-synthesized **g@JUK-8X(op)** to nonporous closed-pore (**cp**) phases, further

https://doi.org/10.1021/acs.chemmater.2c00249
Chem. Mater. XXXX, XXX, XXX−XXX

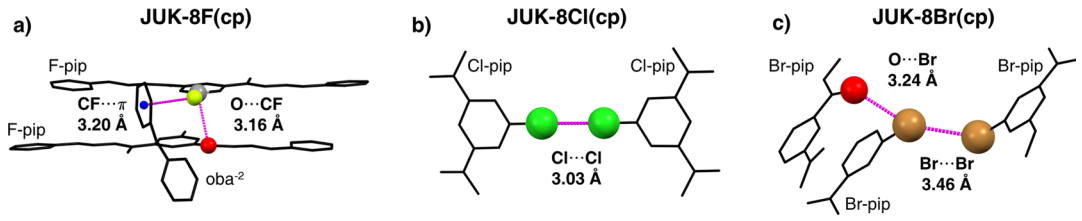

Figure 2. Crystal structures of desolvated phases, determined from PXRD, showing key halogen interactions: (a) CF···π and O···CF interactions in **JUK-8F(cp)**, (b) Cl···Cl interaction in **JUK-8Cl(cp)**, and (c) Br···Br and O···Br interactions in **JUK-8Br(cp)**. F—yellow, Cl—green, Br—brown, O—red, and aromatic centroid—blue.

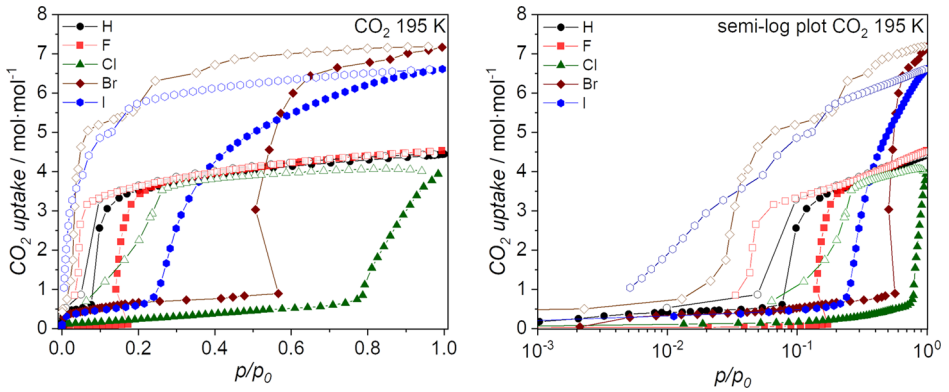

Figure 3. Adsorption isotherms (left) of CO_2 at 195 K for pristine activated $[Zn(oba)(X\text{-}pip)]_n$ (X = H, F, Cl, Br and I), **JUK-8X**. Semilog plot (right) indicating differences in the low-pressure region. The isotherm for **JUK-8** was adapted from the previous work (ref 40). Full symbols—adsorption; open symbols—desorption.

Table 1. Porosity Parameters for Pristine $[Zn(oba)(X\text{-}pip)]_n$ (g@JUK-8X(op)) and Physical Properties of Halogen Atoms

	JUK-8X				
	H	F	Cl	Br	I
maximum uptake/$cm^3 \cdot g^{-1}$ ($mol \cdot mol^{-1}$)	142 (4.4)	143 (4.5)	123 (4.0)	208 (7.2)	170 (6.2)
p_{go}/p_0	0.08	0.17	0.78	0.56	0.22
$\Delta E_{(cp\text{-}op)}$[a]/$kJ \cdot mol^{-1}$	62.8	68.7	74.2	72.9	-[b]
van der Vaals radius/pm	120	140	175	185	198
αD[c]	4.5	3.74 ± 0.08	14.6 ± 0.1	21 ± 1	32.9 ± 1.3

[a]Crystal structures from SC-XRD (**g@JUK-8X(op)**) and PXRD (**JUK-8X(cp)**) data were used for calculations. [b]Due to experimental limitations, we were unable to determine the structure of **JUK-8I(cp)** and calculate the corresponding $\Delta E_{(cp\text{-}op)}$. [c]Static scalar dipole polarizability (in atomic units) for neutral atoms (ref 50).

denoted as **JUK-8X(cp)** (Figure 2). The transition of **g@JUK-8X(op)** (X = H, F, Cl) occurs directly from the **op** to **cp** phase, whereas **g@JUK-8I(op)** exhibits a two-step phase transition. In the case of **g@JUK-8Br(op)**, an additional phase is metastable at the investigated temperature (120 °C), and the mixture of phases is detectable. These observations indicate the essential influence of radius and polarizability of halogen atoms on solvent−framework interactions.

By the combination of computational modeling and Rietveld analysis for PXRD patterns of the desolvated phases, we solved and refined the crystal structures of all **JUK-8X(cp)** MOFs except the iodine derivative (Figures 2 and S8, Supporting Information). The compounds are isostructural to the closed-pore phase of **JUK-8(cp)** whose structure was previously determined from SC-XRD data;[47] however, in contrast to this parental structure, the desolvation of halogen derivatives causes weakening of the $(N-H)_{pip}\cdots O_{oba}$ hydrogen bond (Tables S3 and S4, Supporting Information). The meticulous comparison of the **g@op** and **cp** structures reveals that all eight subnetworks in each MOF shrink to the nonporous **cp** phase upon activation, but halogen substituents have a significant influence on these processes. The activation of **JUK-8F** causes a rearrangement of the zinc coordination sphere and reinforces the interaction between carbon and oxygen (Figure 2), whereas the desolvation of the chlorine derivative breaks the C═O···Cl−C interaction. However, this process leads to the formation of a new interaction between two chlorine atoms from the neighboring subnetworks (Figure 2). In the case of **JUK-8Br(cp)**, the Br···O interaction becomes weaker, as compared to **g@JUK-8Br(op)**, because electron density is transferred from the bromine atom to another bromine atom from the adjacent subnetwork and a new Br···Br interaction is created in the **cp** phase (Figure 2).

2.3. General Remarks on CO_2 Responsiveness of JUK-8X. Free accessible voids of the closed-pore structures **JUK-8X(cp)** are neglectable, occupying 1.9−2.7% volume of the unit cells, and the whole group is nonporous toward N_2 at 77 K (Figure S9, Supporting Information). In contrast, CO_2 molecules at 195 K enter all structures and trigger phase transitions that depend on the halogen substituent (Figure 3

https://doi.org/10.1021/acs.chemmater.2c00249
Chem. Mater. XXXX, XXX, XXX−XXX

Table 2. Unit Cell Parameters for JUK-8F Phases with Corresponding Porosity Data and Transition Energies[a]

	V/Å^3	a/Å	b/Å	c/Å	β/°	space group	V_{pt}/cm^3·g^{-1}	p_w/Å	ΔE/kJ·mol^{-1}
JUK-8F(cp)	6610	13.1	18.2	27.7	93.8	*C*2/*c*	0.017		0
CO_2@JUK-8F(op)	7911	15.8	19.2	26.3	97.7	*Cc*	0.205	2.83	60.8
CO_2@JUK-8F(ip)	6697	13.3	18.3	27.5	94.4	*C*2/*c*	0.050		6.6
g@JUK-8F(op)	8148	16.7	19.3	25.7	100.5	*Cc*	0.272	3.50	68.7

[a] V_{pt}—theoretical accessible pore volume (calculated by Mercury software with a probe radius of 1.65 Å); p_w—pore limiting diameter (calculated by Zeo++); ΔE—calculated transition energy (DFT).

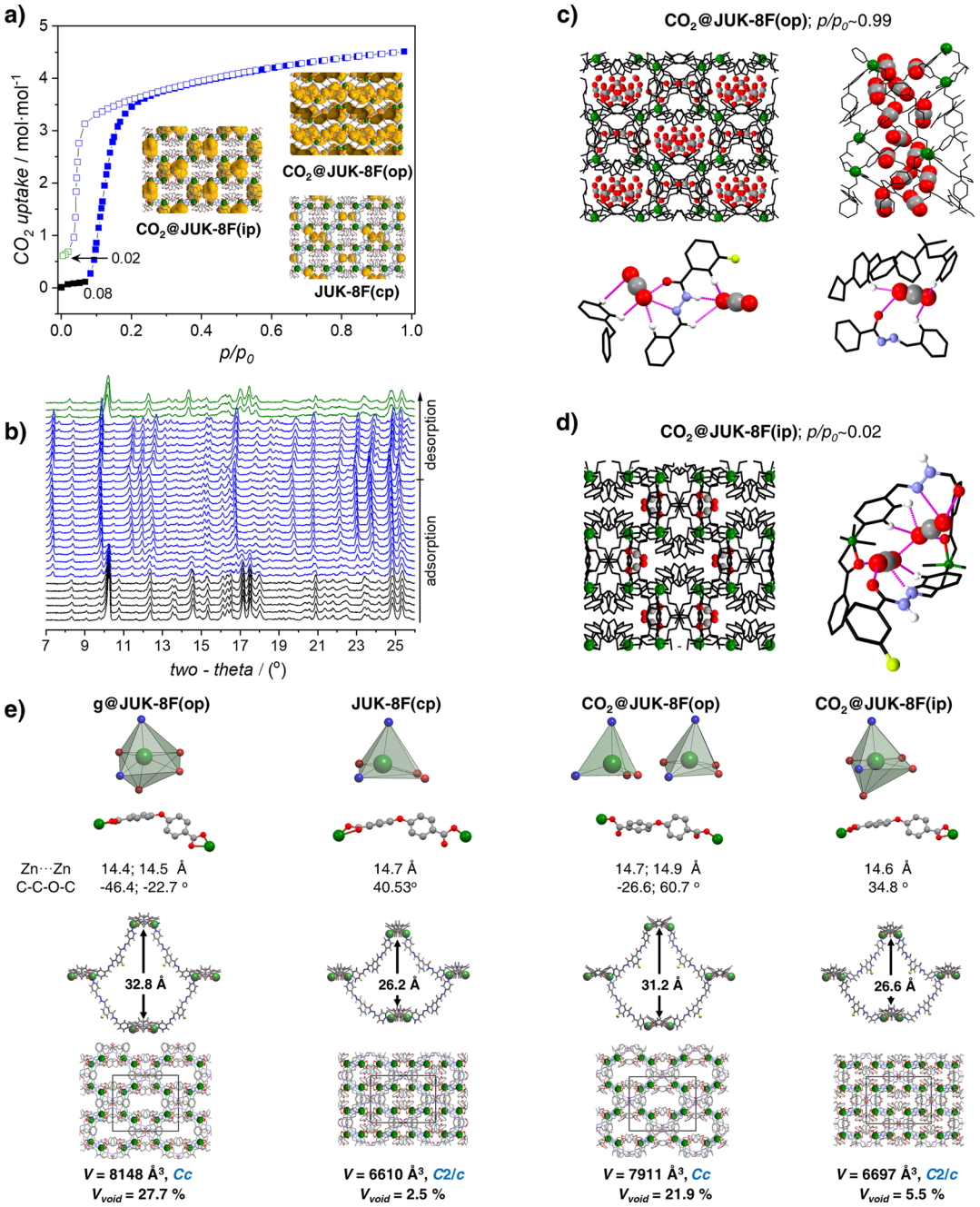

Figure 4. (a) CO_2 adsorption isotherm for **JUK-8F(cp)** at 195 K (second cycle). (b) Corresponding in situ PXRD patterns (λ = 1.540599 Å) measured in the selected points of the isotherm. (c,d) Crystal structures of **CO_2@JUK-8F(op)** and **CO_2@JUK-8F(ip)** refined from in situ PXRD patterns; CO_2 molecules—colored large spheres, interacting atoms—colored small spheres, and the rest of atoms are in black. (e) Crystal structures of **g@JUK-8F(op)**, $[Zn(oba)(F\text{-}pip)]_n$ (**JUK-8F(cp)**), $\{[Zn(oba)(F\text{-}pip)]\cdot 4.5CO_2\}_n$ (**CO_2@JUK-8F(op)**), and $\{[Zn(oba)(F\text{-}pip)]\cdot 0.5CO_2\}_n$ (**CO_2@JUK-8F(ip)**). Zn···Zn—distance between Zn atoms. C−C−O−C—selected torsion angles; for more details see Table S6. Void fractions (V_{void}) were calculated with Mercury software by using a probe molecule with a radius of 1.2 Å. Color codes: Zn—green, O—red, N—blue, H—white, C—gray, F—pale yellow, voids—yellow, and short contacts—magenta.

https://doi.org/10.1021/acs.chemmater.2c00249
Chem. Mater. XXXX, XXX, XXX−XXX

and Table 1). The adsorption-induced pore-opening transition (**cp** → **op**) of all but the fluorine derivative is preceded by an intermediate state **CO_2@JUK-8X(ip)** (X = H, Cl, Br, I). The detailed analysis of the isotherms indicates that the first stage of adsorption for **JUK-8Cl**, **JUK-8Br**, and **JUK-8I** is comparable to that for **JUK-8** (**cp** → **ip**).[47] Carbon dioxide molecules diffuse to the voids localized between two zinc atoms. The different mechanism of adsorption (**cp** → **op**) observed for the fluorine derivative is caused by different internetwork interactions exhibited by its desolvated phase (Figure 2).

In the series of **JUK-8X** frameworks, the gate-opening pressure (p_{go}), defined as a step on the isotherm, ranges from p/p_0 = 0.08 to 0.78, and a simple relationship between p_{go} and a halogen radius is not observed. The detailed comparison of the closed-pore structures (Figure 2) indicates that the Cl···Cl interaction is responsible for an untypical shape of the adsorption isotherm for **JUK-8Cl**, with the highest p_{go} and a tendency to desorb CO_2 molecules at higher pressures compared to other derivatives. A similar effect exists for **JUK-8Br**; however, Br atoms participate in the additional interaction with the oxygen atom which weakens the Br···Br contact.

In the adsorption branches of **JUK-8F** and **JUK-8Br**, we observed the so-called "negative pressure" adsorption profile,[48,49] which is caused by a sudden CO_2 uptake within the open pore phases of MOFs during a volumetric adsorption experiment and by the high cooperativity of the **cp-op** transition. The origin of the phenomenon can be explained by the following: (a) the amount of adsorbed gas exceeds the limited dosing pressure, and in consequence, the pressure drops in the whole system and (b) high kinetical stability of the **ip** and **cp** phases plays a crucial role as well. The finite equilibration time is not sufficient for reaching thermodynamical equilibrium. After exceeding the gate-opening pressure, the measuring system is "forced" by the material in the open form to reduce its pressure to the thermodynamical value.

For a better understanding of the relationship between p_{go} and the nature of halogen atoms, we used density functional theory (DFT) to determine the energy difference, $\Delta E_{(cp\text{-}op)}$, between the experimental desolvated close-pore (**cp**) and solvated open-pore (**op**) structures (Table 1). We have found that $\Delta E_{(cp\text{-}op)}$ is correlated with p_{go}. **JUK-8Cl** shows the highest p_{go} (p_{go}/p_0 = 0.78) and the highest $\Delta E_{(cp\text{-}op)}$ (74.2 kJ·mol^{-1}), while both these values are the lowest for **JUK-8** (p_{go}/p_0 = 0.08; $\Delta E_{(cp\text{-}op)}$ = 62.8 kJ·mol^{-1}). The other derivatives follow the observed trend (Table 1).

During CO_2 desorption, all materials release the majority of adsorbed CO_2 and transform to intermediate states (**ip**) in which CO_2 molecules are trapped in zero-dimensional cages (Figure S10, Supporting Information). Before this state is reached, the unknown phases of $\{[Zn(oba)(X\text{-}pip)]\cdot 5CO_2\}_n$ at $p/p_0 \sim 0.20-0.07$ are detected for the iodine and bromine derivatives. This observation is coherent with the VT-PXRD data (Figure S6, Supporting Information). The desorption data indicate that the strength of interactions between CO_2 and frameworks is correlated with the halogen substituent radius (for the whole series except Cl); in particular, the easiest polarizable and the largest iodine strongly interacts with CO_2 which is manifested by a long tail in the desorption branch for **JUK-8I** (Figure 3 and Table 1).

2.4. In Situ PXRD Monitoring and Computational Studies of CO_2-Induced Phase Transitions. Three materials in the **JUK-8X** series have comparable maximum molar uptakes at a saturation pressure of CO_2 at 195 K. This uptake is practically the same for **JUK-8** and **JUK-8F**, whereas for **JUK-8Cl**, it is smaller by 0.5 CO_2 per zinc center (Table 1 and Figure S11, Supporting Information). Three **JUK-8X** members (X = H, F, Cl) have comparable cell volumes at CO_2 saturation pressure (V = 7817, 7911, and 8117 Å^3 for H, F, and Cl, respectively), and the discrepancy between the adsorption capacity for **JUK-8Cl** compared to the two other derivatives is caused by a coexistence of porous and less porous phases of **JUK-8Cl** at $p/p_0 \sim 0.99$ (see in situ PXRD during CO_2 adsorption, Figure S12, Supporting Information). Despite numerous attempts, we were unable to index the in situ PXRD patterns measured for **JUK-8I** during CO_2 adsorption due to strong X-ray absorption of iodine atoms in the transmission geometry. Nonetheless, we determined the CO_2-triggered transition mechanism of **JUK-8F** and could determine the preferable adsorption sites for CO_2 in the pores (Table 2, Figures 4 and S13, Supporting Information).

When exposed to dynamic vacuum at an elevated temperature, **g@JUK-8F(op)** shrinks to the **cp** phase, the unit cell volume is reduced by 19%, and the space group changes from *Cc* to *C*2/*c*. The observed contraction causes a significant decrease of the *a* unit cell parameter and is accompanied by moderate alterations of *b*, *c*, and *β*. The closed-pore framework, exposed to gaseous CO_2 at 195 K, transforms directly to the **op** phase in which its cell volume (7911 Å^3) increases by 23% relative to the **cp** structure. The accommodation of CO_2 molecules induces the symmetry reduction from *C*2/*c* to *Cc*. Notably, the unsubstituted **JUK-8** maintains the space group (*C*2/*c*) during the adsorption of CO_2 at 195 K (Table S5, Supporting Information). The absence of an intermediate phase in the adsorption branch for **JUK-8F**, contrary to the other **JUK-8X** materials, is caused by the enhancement of FC···O and CF···p interactions in the **cp** phase and by a considerable distortion of the coordination sphere of zinc (see Figures 2 and 4). These interactions "freeze" the framework deformations during the interaction with CO_2 and hinder diffusion of gas molecules at low pressures.

After exceeding p_{go} at p/p_0 = 0.17, **JUK-8F(cp)** opens to the **CO_2@JUK-8F(op)** phase, whose structure can be compared with another open-pore as-synthesized phase, **g@JUK-8F(op)**. Despite a slight difference (237 Å^3) between cell volumes of open-pore structures, that is, **CO_2@JUK-8F(op)** and the solvent loaded **g@JUK-8F(op)**, their pore geometries are significantly different. In particular, the pore limiting diameter for **g@JUK-8F(op)** is larger by 0.7 Å than that of the fully CO_2-loaded framework (Figure S13, Supporting Information). These observations indicate a remarkable ability of the whole **JUK-8X** platform to adapt its structure to the guest molecule.

At a saturation pressure, distinctive positions of CO_2 molecules were determined for **CO_2@JUK-8F(op)** (Figure 4c). Most of these molecules are localized in 1D channels where they interact with the framework and with each other, whereas two carbon dioxide molecules per two inequivalent zinc atoms rest in a more confined space (Figures S13−S15, Supporting Information). Notably, the acylhydrazone linkers create three different binding sites in the framework (Figure 4c). In the desorption branch, **CO_2@JUK-8F(op)** releases four CO_2 molecules per zinc which triggers a phase transition to **CO_2@JUK-8F(ip)** accompanied by an increase of space group symmetry (*Cc* → *C*2/*c*). The remaining CO_2 molecules

https://doi.org/10.1021/acs.chemmater.2c00249
Chem. Mater. XXXX, XXX, XXX−XXX

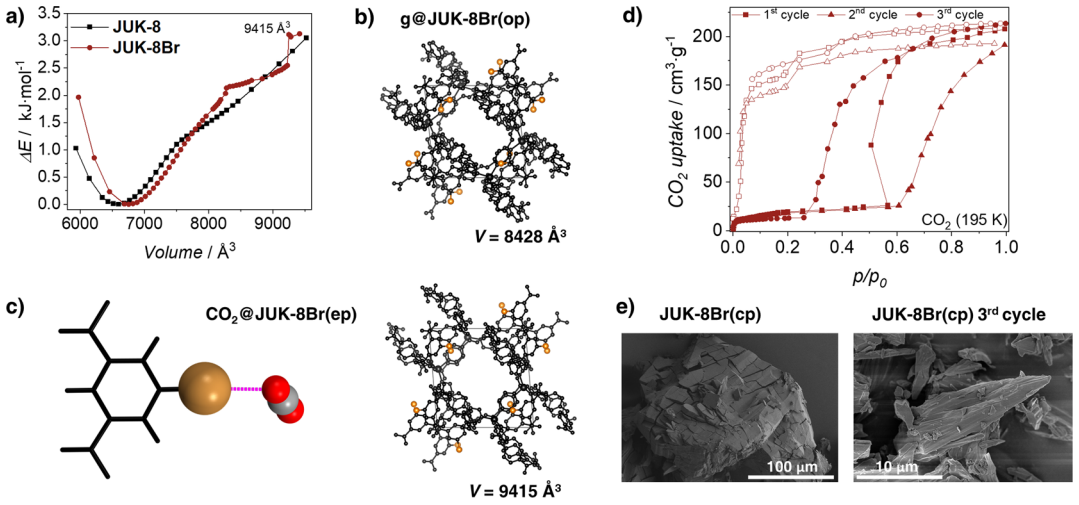

Figure 5. (a) Change of the energy (DFT calculations) as a function of volume for **JUK-8** and **JUK-8Br**. (b) Single-crystal structure of the solvated **g@JUK-8Br(op)** phase. (c) DFT-calculated extended pore structure of **JUK-8Br(ep)**; Br—brown, O—red, and C—gray. Data for **JUK-8** were adapted from the previously published study (ref 40). (d) Stability of porosity upon repeated CO_2 adsorption (full symbols) and desorption (open symbols) at 195 K. (e) SEM image of the desolvated **JUK-8Br(cp)** sample compared with the SEM image taken after the third CO_2 adsorption/desorption cycle.

are trapped in the vicinity of the acylhydrazone group (Figure 4d).

In order to have a deeper understanding of the observed phenomena, we calculated the energy of transition between the four known phases of **JUK-8F** (Table 2). All experimental structures were optimized with a fixed volume, then guest molecules were removed from the unit cells, and the internal energy was calculated using the DFT method. One can see that the energy required for transforming the **cp** to **ip** structure is approximately 1 order of magnitude lower than the energy required for full opening of **JUK-8F**. We recently showed that temperature has a very limited impact on the energetic landscape of the **JUK-8** framework,[51] and hence the energy differences presented in Table 2 will not be significantly changed when the temperature contribution is considered (195 K—temperature during adsorption). The small energy difference between **CO_2@JUK-8F(op)** and **g@JUK-8F(op)** confirms the adaptation capabilities of **JUK-8X** frameworks.

The Le Bail fits of the in situ measured PXRD patterns of **JUK-8Br** under CO_2 saturation shed light on the global structural changes during carbon dioxide adsorption. In the first stage, the material adsorbs 0.5 CO_2 molecules per zinc and transforms to the **ip** phase, $\{[Zn(oba)(Br\text{-}pip)]\cdot 0.5CO_2\}_n$. Above $p/p_0 \sim 0.62$, **CO_2@JUK-8Br(ip)** transforms to an expanded phase, **CO_2@JUK-8Br(ep)**, and enormous (by 38.1%) expansion of the cell volume to 9322 Å^3 is observed, which is 1411 Å^3 larger compared to **CO_2@JUK-8F(op)**. The first peak in the PXRD pattern of **CO_2@JUK-8Br(ep)** collected at $p/p_0 \sim 0.99$ has a considerably lower value, 2θ = 6.1°, compared to those of the pristine **g@JUK-8Br(op)** (6.9°) and **CO_2@JUK-8F(op)** (7.3°) phases. A similar effect is observed in the pattern of **JUK-8I** at CO_2 saturation pressure (2θ = 6.1°). However, in this case, the maximum molar uptake is slightly lower due to the bigger size of iodine compared to bromine. Thus, we assume that iodine has a comparable influence on adsorption properties of the **JUK-8X** series as bromine.

We observe that the experimental unit cell volume of **CO_2@JUK-8Br(ep)** is larger (9322 Å) than the corresponding value for **CO_2@JUK-8F(op)** (7911 Å), and additional interactions that immobilize CO_2 molecules in **CO_2@JUK-8Br(ep)** are identified. Following these observations, we constructed energy profiles from the optimized **g@JUK-8Br(op)** and **JUK-8Br(cp)** crystal structures according to the protocol applied in the previous studies.[40,52] The experimental **cp** and **op** structures were inter- and extrapolated to create a set of unit cells with volumes varying from 6000 to 9450 Å^3 which were later optimized with constrained volumes using DFT methodology.[40,51,53,54] The difference between the energy−volume relation for **JUK-8** and **JUK-8Br** is shown in Figure 5. Apart from the expected increase of the volume of a stable closed pore structure from 6600 Å^3 in the case of **JUK-8** to 6754 Å^3 for **JUK-8Br**, we also observe the change of the energy profile at higher volumes. In contrast to the parental platform, where only two significant volume ranges appear (harmonic up to 7504 Å^3 and quasi-linear above), the profile for the bromine derivative has a significant step at high volumes (9415 Å^3), which is comparable to the experimental value equal to 9322 Å^3 from the Le Bail fit. It corresponds to the structural transformation responsible for the observed adsorption properties. Comparing the experimental DMF-loaded **op** phase (V = 8428 Å^3) to the **ep** phase (V = 9415 Å^3), we observe the increase of the helium void fraction from 0.25 to 0.35 (Figure S16).

To assure the most accurate agreement between simulation and experiment data, we inserted seven CO_2 molecules per unit formula (the value corresponding to the experimental uptake at saturation pressure) into the pore and optimized the unit cell using DFT. We found that CO_2 molecules are engaged in halogen interaction with the bromine atom of the *Br-pip* linker. To get a deeper understanding of the role of halogen substituents, we calculated the energy differences ΔE between stable (**cp**) and hypothetical metastable (**ep**) phases of **JUK-8X**. The results, presented in Table 3 show that the probability of existence of both JUK-8 and JUK-8F frameworks in the **ep** phase is extremely low, mainly due to high energy penalty (ΔE > 2200 kJ·mol^{-1}).

Following our recent studies, neither temperature (vibrational free energy) nor adsorption of CO_2 (adsorption potential) contribution can balance such a significant energy

https://doi.org/10.1021/acs.chemmater.2c00249
Chem. Mater. XXXX, XXX, XXX−XXX

Table 3. Calculated Energy Difference between Stable (cp) and Hypothetical Metastable (ep) Phases of JUK-8X

	JUK-8	JUK-8F	JUK-8Cl	JUK-8Br	JUK-8I
$\Delta E_{(ep\text{-}cp)}$/kJ·mol^{-1}	2235.4	2555.3	314.0	301.8	267.1

difference. The changes of $\Delta E_{(ep\text{-}cp)}$ calculated for various halogen derivatives suggest that the stability of different phases in the **JUK-8X** series is regulated by the subtle interplay between host−guest interactions and halogen steric hindrance.

One must keep in mind that the applied theoretical approach has limitations, for example, the dynamics of the adsorbate and the framework is neglected in our calculations.

2.5. Tolerance of JUK-8Br Toward Repeatable Adsorption−Desorption Stress. In previous reports,[40,47] we have shown that **JUK-8** maintains the structure and properties upon applying mechanical force, boiling in water, as well as upon exposition to a repeatable adsorption stress. According to the experiment and theory, the cell volume of **JUK-8Br** during CO_2 adsorption increases significantly (38.1%) compared to **JUK-8**, **JUK-8F**, or **JUK-8Cl** (17−23%). It indicates that the bromine derivative experiences substantial mechanical stress during accommodation of the adsorbate, which may influence its adsorption properties.

We have carried out three cycles of CO_2 adsorption−desorption by **JUK-8Br** (Figure 5). During the second adsorption−desorption cycle, p_{go} slightly increases, while the maximum uptake drops from 207 to 191 cm^3·g^{-1}. However, in the third cycle, the gate-opening pressure drops significantly to p/p_0 = 0.26, but the maximal uptake reaches 213 cm^3·g^{-1}. We assume that the observed fluctuations of both p_{go} and the maximal uptake are connected to the crystal size of the adsorbent. To verify this hypothesis, we have recorded scanning electron microscopy (SEM) images of the desolvated **JUK-8Br(cp)** sample before and after three cycles of adsorption and desorption. The images confirm that the crystal size of the activated material is ca. 10 times bigger compared to the material exposed to the repeatable mechanical stress (Figures 5 and S17, Supporting Information).

In addition, we have checked the stability of the whole series in organic solvents including methanol, acetone, and ethyl acetate (Figure S18, Supporting Information). The ex situ PXRD patterns recorded for the samples immersed for 48 h indicate that all **JUK-8X** are stable in methanol, while only **JUK-8I** is unstable in acetone and ethyl acetate.

3. CONCLUSIONS

In summary, in this work, we have achieved control over the stimuli-responsiveness of the **JUK-8** platform by introducing halogen substituents in the diacylhydrazone (*pip*) linker. The crystal structures of solvated, desolvated, and CO_2-loaded phases, derived from SC-XRD and in situ PXRD experiments under gas loading, combined with the spectroscopy and DFT calculations allow us to understand the switching mechanism and highlight the crucial roles in spatial adaptability of **JUK-8X** isoreticular series to carbon dioxide at 195 K. The Cl···Cl interaction which exists in the closed-pore phase of **JUK-8Cl** gives rise to the highest gate-opening and closing pressure in the **JUK-8X** derivatives, whereas the reinforcement of O···CF interaction, connected with the change of the coordination number of zinc in the fluorine derivative, is accountable for the different adsorption−desorption mechanism for **JUK-8F** (**cp** → **op** adsorption followed by **op** → **ip** desorption) than for other **JUK-8X** (X = H, Cl, Br, I) materials (**cp** → **ip** → **op** adsorption followed by **op** → **ip** desorption). In the case of **JUK-8F**, we determined the mechanism and energetical landscape of CO_2-induced transitions with preferable adsorption sites for CO_2 in the pores. In a fully CO_2-loaded **JUK-8F**, the CO_2 molecules occupy 1D channels and more confined spaces. During desorption, the shrinking structure of **JUK-8F** traps CO_2 molecules in the vicinity of acylhydrazone groups.

Larger bromine or iodine substituents increase the maximum molar uptake of CO_2 by 59 and 48%, respectively, as compared to the parental **JUK-8** structure. Due to experimental limitations, we shed light on the microscopic mechanism of **JUK-8Br** phase transitions using computational approach by the analysis of the energetics of the phenomenon. To assure accurate probing of the adsorption-induced changes, our computational model considers in situ PXRD patterns measured under CO_2 loading. With the so-constructed DFT simulations, we showed differences between the adsorption-induced pore-opening transition trajectories for **JUK-8** and **JUK-8Br**. Based on the in silico designed and characterized **ep** phase of the bromine derivative, we proposed an explanation of the counterintuitive increased maximum molar uptake in Br- and I- based MOFs. Overall, the presented utilization of halogen interaction for controlling the response of the **JUK-8X** system can be transferred to other materials, while further development of described computational methodology may be leveraged to different complex cases of flexible MOFs.

4. EXPERIMENTAL SECTION

4.1. Synthesis of X-pip Linkers. Each *X-pip* linker from the series (X = Cl, Br, I) was obtained in several steps starting from 5-aminoisophthalic acid that was subsequently converted to the corresponding 5-haloisophthalic acid, its dimethyl ester, the corresponding hydrazide, and finally to the diacylhydrazone *X-pip* linker. The *F-pip* was obtained in the same manner with the only difference being that dimethyl 5-fluoroisophthalate was directly synthesized from dimethyl 5-aminoisophthalate that was obtained from 5-aminoisophtalic acid. The identity and purity of each intermediate were confirmed by NMR spectroscopy. The synthetic details with spectroscopic data can be found in the Supporting Information.

4.2. Synthesis of g@JUK-8X(op). $Zn(NO_3)_2{\cdot}6H_2O$ (0.30 mmol), *X-pip* (0.30 mmol), and 4,4′-oxybis(benzenedicarboxylic) acid (H_2oba) (0.30 mmol) were suspended in DMF (5.4 mL) and H_2O (0.6 mL) by sonication (60 s) and heated in a closed pyrex vial (10 mL) at 80 °C for 2 days. Pale yellow crystals of **g@JUK-8X(op)** were filtered off, washed with DMF, and dried.

Suitable single crystals of **g@JUK-8X(op)** (X = F, Br) were selected from the bulk. **g@JUK-8Cl(op)**: $Zn(NO_3)_2{\cdot}6H_2O$ (0.075 mmol), *Cl-pip* (0.075 mmol), and 4,4′-oxybis(benzenedicarboxylic) acid (H_2oba) (0.075 mmol); **g@JUK-8I(op)**: $Zn(NO_3)_2{\cdot}6H_2O$ (0.10 mmol), *I-pip* (0.10 mmol), and 4,4′-oxybis(benzenedicarboxylic) acid (H_2oba) (0.10 mmol). In both cases, the reagents were suspended in DMF (2.6 mL) and H_2O (0.4 mL) by sonication (60 s) and heated in a closed vial (4 mL) at 80 °C for 4 days.

4.3. Methods. The details of measurements including elemental and thermogravimetric analyses, ex situ and in situ powder X-ray diffraction, gas physisorption measurements, NMR spectroscopy, SEM analysis, and SC-XRD as well as the details of computational simulations can be found in the Supporting Information.

■ ASSOCIATED CONTENT

Supporting Information

The Supporting Information is available free of charge at https://pubs.acs.org/doi/10.1021/acs.chemmater.2c00249.

https://doi.org/10.1021/acs.chemmater.2c00249
Chem. Mater. XXXX, XXX, XXX−XXX

CrystallographicCrystallographic data (SC-XRD) for **g@JUK-8F(op)** (CIF)
Crystallographic data (SC-XRD) for **g@JUK-8Cl(op)** (CIF)
Crystallographic data (SC-XRD) for **g@JUK-8Br(op)** (CIF)
Crystallographic data (SC-XRD) for **g@JUK-8I** (CIF)
Crystallographic data (PXRD) for **JUK-8F(cp)** (CIF)
Crystallographic data (PXRD) for **CO_2@JUK-8F(op)** (CIF)
Crystallographic data (PXRD) for **CO_2@JUK-8F(ip)** (CIF)
Crystallographic data (PXRD) for **JUK-8Cl(cp)** (CIF)
Crystallographic data (PXRD) for **JUK-8Br(cp)** (CIF)
Crystallographic data (simulated) for **CO_2@JUK-8Br-(ep)** (CIF)
Adsorption data for **JUK-8F-CO_2-195K** (TXT)
Adsorption data for **JUK-8Cl-CO_2-195K** (TXT)
Adsorption data for **JUK-8Br-CO_2-195K** (TXT)
Adsorption data for **JUK-8I-CO_2-195K** (TXT)
Adsorption data for **JUK-8H-CO_2-195K** (TXT)
Details of synthetic procedures and methods, additional experimental data including physisorption measurements, PXRD patterns, crystal structure drawings, powder X-ray structures, calculated structure, and adsorption information files (PDF)

AUTHOR INFORMATION

Corresponding Authors

Kornel Roztocki − *Faculty of Chemistry, Adam Mickiewicz University, 61-614 Poznań, Poland; Center for Advanced Technology, Adam Mickiewicz University, 61-614 Poznań, Poland;* orcid.org/0000-0001-7102-9802; Email: kornel.roztocki@amu.edu.pl

Dariusz Matoga − *Faculty of Chemistry, Jagiellonian University, 30-387 Kraków, Poland;* orcid.org/0000-0002-0064-5541; Email: dariusz.matoga@uj.edu.pl

Authors

Filip Formalik − *Department of Micro, Nano, and Bioprocess Engineering, Faculty of Chemistry, Wroclaw University of Science and Technology, 50-370 Wroclaw, Poland; Department of Theoretical Physics, Faculty of Fundamental Problems of Technology, Wroclaw University of Science and Technology, 50-370 Wroclaw, Poland;* orcid.org/0000-0003-3981-3298

Volodymyr Bon − *Chair of Inorganic Chemistry, Technische Universität Dresden, 01062 Dresden, Germany;* orcid.org/0000-0002-9851-5031

Anna Krawczuk − *Institute of Inorganic Chemistry, Georg-August-University Göttingen, 37077 Göttingen, Germany; Faculty of Chemistry, Jagiellonian University, 30-387 Kraków, Poland;* orcid.org/0000-0001-7172-7264

Piotr Goszczycki − *Faculty of Chemistry, Jagiellonian University, 30-387 Kraków, Poland*

Bogdan Kuchta − *Department of Micro, Nano, and Bioprocess Engineering, Faculty of Chemistry, Wroclaw University of Science and Technology, 50-370 Wroclaw, Poland; MADIREL, CNRS, Aix-Marseille University, 13397 Marseille, France;* orcid.org/0000-0002-8635-4154

Stefan Kaskel − *Chair of Inorganic Chemistry, Technische Universität Dresden, 01062 Dresden, Germany;* orcid.org/0000-0003-4572-0303

Complete contact information is available at: https://pubs.acs.org/10.1021/acs.chemmater.2c00249

Notes

The authors declare no competing financial interest.

ACKNOWLEDGMENTS

We gratefully acknowledge the support of the National Science Centre (NCN), Poland (grant nos. 2020/36/C/ST4/00534, K.R.; and 2019/35/B/ST5/01067, D.M.). S.K. acknowledges support by the DFG (FOR2433). V.B. thanks BMBF (project no. 05K19OD2) for the financial support. This research was supported in part by PL-Grid Infrastructure.

REFERENCES

(1) Li, H.; Eddaoudi, M.; O'Keeffe, M.; Yaghi, O. M. Design and Synthesis of an Exceptionally Stable and Highly Porous Metal-Organic Framework. *Nature* **1999**, *402*, 276.
(2) Chui, S. S.-Y.; Lo, S. M.-F.; Charmant, J. P. H.; Orpen, A. G.; Williams, I. D. A Chemically Functionalizable Nanoporous Material [Cu3(TMA)2(H2O)3]n. *Science* **1999**, *283*, 1148−1150.
(3) Cavka, J. H.; Jakobsen, S.; Olsbye, U.; Guillou, N.; Lamberti, C.; Bordiga, S.; Lillerud, K. P. A New Zirconium Inorganic Building Brick Forming Metal Organic Frameworks with Exceptional Stability. *J. Am. Chem. Soc.* **2008**, *130*, 13850−13851.
(4) Barthelet, K.; Marrot, J.; Riou, D.; Férey, G. A Breathing Hybrid Organic−Inorganic Solid with Very Large Pores and High Magnetic Characteristics. *Angew. Chem., Int. Ed.* **2002**, *41*, 281−284.
(5) Kitaura, R.; Seki, K.; Akiyama, G.; Kitagawa, S. Porous Coordination-Polymer Crystals with Gated Channels Specific for Supercritical Gases. *Angew. Chem., Int. Ed.* **2003**, *42*, 428−431.
(6) Maspoch, D.; Ruiz-Molina, D.; Wurst, K.; Domingo, N.; Cavallini, M.; Biscarini, F.; Tejada, J.; Rovira, C.; Veciana, J. A Nanoporous Molecular Magnet with Reversible Solvent-Induced Mechanical and Magnetic Properties. *Nat. Mater.* **2003**, *2*, 190−195.
(7) Sato, H.; Kosaka, W.; Matsuda, R.; Hori, A.; Hijikata, Y.; Belosludov, R. V.; Sakaki, S.; Takata, M.; Kitagawa, S. Self-Accelerating CO Sorption in a Soft Nanoporous Crystal. *Science* **2014**, *343*, 167−170.
(8) Krause, S.; Bon, V.; Senkovska, I.; Stoeck, U.; Wallacher, D.; Többens, D. M.; Zander, S.; Pillai, R. S.; Maurin, G.; Coudert, F.-X.; Kaskel, S. A Pressure-Amplifying Framework Material with Negative Gas Adsorption Transitions. *Nature* **2016**, *532*, 348.
(9) Katsoulidis, A. P.; Antypov, D.; Whitehead, G. F. S.; Carrington, E. J.; Adams, D. J.; Berry, N. G.; Darling, G. R.; Dyer, M. S.; Rosseinsky, M. J. Chemical Control of Structure and Guest Uptake by a Conformationally Mobile Porous Material. *Nature* **2019**, *565*, 213−217.
(10) Kitagawa, S.; Kitaura, R.; Noro, S.-i. Functional Porous Coordination Polymers. *Angew. Chem., Int. Ed.* **2004**, *43*, 2334−2375.
(11) Férey, G.; Serre, C. Large Breathing Effects in Three-Dimensional Porous Hybrid Matter: Facts, Analyses, Rules and Consequences. *Chem. Soc. Rev.* **2009**, *38*, 1380−1399.
(12) Schneemann, A.; Bon, V.; Schwedler, I.; Senkovska, I.; Kaskel, S.; Fischer, R. A. Flexible Metal−Organic Frameworks. *Chem. Soc. Rev.* **2014**, *43*, 6062−6096.
(13) Sarkisov, L.; Martin, R. L.; Haranczyk, M.; Smit, B. On the Flexibility of Metal−Organic Frameworks. *J. Am. Chem. Soc.* **2014**, *136*, 2228−2231.
(14) Chang, Z.; Yang, D.-H.; Xu, J.; Hu, T.-L.; Bu, X.-H. Flexible Metal−Organic Frameworks: Recent Advances and Potential Applications. *Adv. Mater.* **2015**, *27*, 5432−5441.
(15) Seth, S.; Jhulki, S. Porous Flexible Frameworks: Origins of Flexibility and Applications. *Mater. Horiz.* **2021**, *8*, 700−727.
(16) Li, Z. H.; Zeng, H.; Zeng, G.; Ru, C.; Li, G.; Yan, W.; Shi, Z.; Feng, S. Multivariate Synergistic Flexible Metal-Organic Frameworks

with Superproton Conductivity for Direct Methanol Fuel Cells. *Angew. Chem., Int. Ed.* **2021**, *60*, 26577−26581.
(17) Chen, X.; Xie, H.; Lorenzo, E. R.; Zeman, C. J.; Qi, Y.; Syed, Z. H.; Stone, A. E. B. S.; Wang, Y.; Goswami, S.; Li, P.; Islamoglu, T.; Weiss, E. A.; Hupp, J. T.; Schatz, G. C.; Wasielewski, M. R.; Farha, O. K. Direct Observation of Modulated Radical Spin States in Metal−Organic Frameworks by Controlled Flexibility. *J. Am. Chem. Soc.* **2022**, *144*, 2685−2693.
(18) Chong, S.; Rogge, S. M. J.; Kim, J. Tunable Electrical Conductivity of Flexible Metal-Organic Frameworks. *Chem. Mater.* **2022**, *34*, 254−265.
(19) Thallapally, P. K.; Tian, J.; Radha Kishan, M.; Fernandez, C. A.; Dalgarno, S. J.; McGrail, P. B.; Warren, J. E.; Atwood, J. L. Flexible (Breathing) Interpenetrated Metal−Organic Frameworks for CO2 Separation Applications. *J. Am. Chem. Soc.* **2008**, *130*, 16842−16843.
(20) Matsuda, R. Selectivity from Flexibility. *Nature* **2014**, *509*, 434−435.
(21) Taylor, M. K.; Runčevski, T.; Oktawiec, J.; Bachman, J. E.; Siegelman, R. L.; Jiang, H.; Mason, J. A.; Tarver, J. D.; Long, J. R. Near-Perfect CO2/CH4 Selectivity Achieved through Reversible Guest Templating in the Flexible Metal−Organic Framework Co(Bdp). *J. Am. Chem. Soc.* **2018**, *140*, 10324−10331.
(22) Li, L.; Lin, R.-B.; Krishna, R.; Wang, X.; Li, B.; Wu, H.; Li, J.; Zhou, W.; Chen, B. Flexible−Robust Metal−Organic Framework for Efficient Removal of Propyne from Propylene. *J. Am. Chem. Soc.* **2017**, *139*, 7733−7736.
(23) Mason, J. A.; Oktawiec, J.; Taylor, M. K.; Hudson, M. R.; Rodriguez, J.; Bachman, J. E.; Gonzalez, M. I.; Cervellino, A.; Guagliardi, A.; Brown, C. M.; Llewellyn, P. L.; Masciocchi, N.; Long, J. R. Methane Storage in Flexible Metal−Organic Frameworks with Intrinsic Thermal Management. *Nature* **2015**, *527*, 357.
(24) Carrington, E. J.; McAnally, C. A.; Fletcher, A. J.; Thompson, S. P.; Warren, M.; Brammer, L. Solvent-Switchable Continuous-Breathing Behaviour in a Diamondoid Metal−Organic Framework and Its Influence on CO2 versus CH4 Selectivity. *Nat. Chem.* **2017**, *9*, 882.
(25) Yang, Q. Y.; Lama, P.; Sen, S.; Lusi, M.; Chen, K. J.; Gao, W. Y.; Shivanna, M.; Pham, T.; Hosono, N.; Kusaka, S.; Perry, J. J.; Ma, S.; Space, B.; Barbour, L. J.; Kitagawa, S.; Zaworotko, M. J. Reversible Switching between Highly Porous and Nonporous Phases of an Interpenetrated Diamondoid Coordination Network That Exhibits Gate-Opening at Methane Storage Pressures. *Angew. Chem., Int. Ed.* **2018**, *57*, 5684−5689.
(26) Taylor, M. K.; Runčevski, T.; Oktawiec, J.; Gonzalez, M. I.; Siegelman, R. L.; Mason, J. A.; Ye, J.; Brown, C. M.; Long, J. R. Tuning the Adsorption-Induced Phase Change in the Flexible Metal−Organic Framework Co(Bdp). *J. Am. Chem. Soc.* **2016**, *138*, 15019−15026.
(27) Zhu, A. X.; Yang, Q. Y.; Mukherjee, S.; Kumar, A.; Deng, C. H.; Bezrukov, A. A.; Shivanna, M.; Zaworotko, M. J. Tuning the Gate-Opening Pressure in a Switching Pcu Coordination Network, X-Pcu-5-Zn, by Pillar-Ligand Substitution. *Angew. Chem., Int. Ed.* **2019**, *58*, 18212−18217.
(28) Klein, N.; Hoffmann, H. C.; Cadiau, A.; Getzschmann, J.; Lohe, M. R.; Paasch, S.; Heydenreich, T.; Adil, K.; Senkovska, I.; Brunner, E.; Kaskel, S. Structural Flexibility and Intrinsic Dynamics in the M2(2,6-Ndc)2(Dabco) (M = Ni, Cu, Co, Zn) Metal−Organic Frameworks. *J. Mater. Chem.* **2012**, *22*, 10303−10312.
(29) Devic, T.; Horcajada, P.; Serre, C.; Salles, F.; Maurin, G.; Moulin, B.; Heurtaux, D.; Clet, G.; Vimont, A.; Grenèche, J.-M.; Ouay, B. L.; Moreau, F.; Magnier, E.; Filinchuk, Y.; Marrot, J.; Lavalley, J.-C.; Daturi, M.; Férey, G. Functionalization in Flexible Porous Solids: Effects on the Pore Opening and the Host−Guest Interactions. *J. Am. Chem. Soc.* **2010**, *132*, 1127−1136.
(30) Horcajada, P.; Salles, F.; Wuttke, S.; Devic, T.; Heurtaux, D.; Maurin, G.; Vimont, A.; Daturi, M.; David, O.; Magnier, E.; Stock, N.; Filinchuk, Y.; Popov, D.; Riekel, C.; Férey, G.; Serre, C. How Linker's Modification Controls Swelling Properties of Highly Flexible Iron(III) Dicarboxylates MIL-88. *J. Am. Chem. Soc.* **2011**, *133*, 17839−17847.
(31) Ramsahye, N. A.; Trung, T. K.; Bourrelly, S.; Yang, Q.; Devic, T.; Maurin, G.; Horcajada, P.; Llewellyn, P. L.; Yot, P.; Serre, C.; Filinchuk, Y.; Fajula, F.; Férey, G.; Trens, P. Influence of the Organic Ligand Functionalization on the Breathing of the Porous Iron Terephthalate Metal Organic Framework Type Material upon Hydrocarbon Adsorption. *J. Phys. Chem. C* **2011**, *115*, 18683−18695.
(32) Henke, S.; Schneemann, A.; Wütscher, A.; Fischer, R. A. Directing the Breathing Behavior of Pillared-Layered Metal−Organic Frameworks via a Systematic Library of Functionalized Linkers Bearing Flexible Substituents. *J. Am. Chem. Soc.* **2012**, *134*, 9464−9474.
(33) Sakata, Y.; Furukawa, S.; Kondo, M.; Hirai, K.; Horike, N.; Takashima, Y.; Uehara, H.; Louvain, N.; Meilikhov, M.; Tsuruoka, T.; Isoda, S.; Kosaka, W.; Sakata, O.; Kitagawa, S. Shape-Memory Nanopores Induced in Coordination Frameworks by Crystal Downsizing. *Science* **2013**, *339*, 193−196.
(34) Cheng, Y.; Kajiro, H.; Noguchi, H.; Kondo, A.; Ohba, T.; Hattori, Y.; Kaneko, K.; Kanoh, H. Tuning of Gate Opening of an Elastic Layered Structure MOF in CO2 Sorption with a Trace of Alcohol Molecules. *Langmuir* **2011**, *27*, 6905−6909.
(35) Kundu, T.; Wahiduzzaman, M.; Shah, B. B.; Maurin, G.; Zhao, D. Solvent-Induced Control over Breathing Behavior in Flexible Metal−Organic Frameworks for Natural-Gas Delivery. *Angew. Chem., Int. Ed.* **2019**, *58*, 8073−8077.
(36) Pedireddi, V. R.; Reddy, D. S.; Goud, B. S.; Craig, D. C.; Rae, A. D.; Desiraju, G. R. The Nature of Halogen···Halogen Interactions and the Crystal Structure of 1,3,5,7-Tetraiodoadamantane. *J. Chem. Soc., Perkin Trans. 2* **1994**, *11*, 2353−2360.
(37) Lommerse, J. P. M.; Stone, A. J.; Taylor, R.; Allen, F. H. The Nature and Geometry of Intermolecular Interactions between Halogens and Oxygen or Nitrogen. *J. Am. Chem. Soc.* **1996**, *118*, 3108−3116.
(38) Yuan, Y.; Li, J.; Sun, X.; Li, G.; Liu, Y.; Verma, G.; Ma, S. Indium−Organic Frameworks Based on Dual Secondary Building Units Featuring Halogen-Decorated Channels for Highly Effective CO2 Fixation. *Chem. Mater.* **2019**, *31*, 1084−1091.
(39) Oppenheim, J. J.; Mancuso, J. L.; Wright, A. M.; Rieth, A. J.; Hendon, C. H.; Dincă, M. Divergent Adsorption Behavior Controlled by Primary Coordination Sphere Anions in the Metal−Organic Framework Ni2X2BTDD. *J. Am. Chem. Soc.* **2021**, *143*, 16343−16347.
(40) Roztocki, K.; Formalik, F.; Krawczuk, A.; Senkovska, I.; Kuchta, B.; Kaskel, S.; Matoga, D. Collective Breathing in an Eightfold Interpenetrated Metal−Organic Framework: From Mechanistic Understanding towards Threshold Sensing Architectures. *Angew. Chem., Int. Ed.* **2020**, *59*, 4491−4497.
(41) Roztocki, K.; Senkovska, I.; Kaskel, S.; Matoga, D. Carboxylate−Hydrazone Mixed-Linker Metal−Organic Frameworks: Synthesis, Structure, and Selective Gas Adsorption. *Eur. J. Inorg. Chem.* **2016**, *2016*, 4450−4456.
(42) Roztocki, K.; Szufla, M.; Hodorowicz, M.; Senkovska, I.; Kaskel, S.; Matoga, D. Introducing a Longer versus Shorter Acylhydrazone Linker to a Metal−Organic Framework: Parallel Mechanochemical Approach, Nonisoreticular Structures, and Diverse Properties. *Cryst. Growth Des.* **2019**, *19*, 7160−7169.
(43) Roztocki, K.; Szufla, M.; Bon, V.; Senkovska, I.; Kaskel, S.; Matoga, D. Interlinker Hydrogen Bonds Govern CO2 Adsorption in a Series of Flexible 2D Diacylhydrazone/Isophthalate-Based MOFs: Influence of Metal Center, Linker Substituent, and Activation Temperature. *Inorg. Chem.* **2020**, *59*, 10717−10726.
(44) Parmar, B.; Patel, P.; Pillai, R. S.; Kureshy, R. I.; Khan, N.-u. H.; Suresh, E. Efficient Catalytic Conversion of Terminal/Internal Epoxides to Cyclic Carbonates by Porous Co(II) MOF under Ambient Conditions: Structure−Property Correlation and Computational Studies. *J. Mater. Chem. A* **2019**, *7*, 2884−2894.

https://doi.org/10.1021/acs.chemmater.2c00249
Chem. Mater. XXXX, XXX, XXX−XXX

(45) Blatov, V. A.; Shevchenko, A. P.; Proserpio, D. M. Applied Topological Analysis of Crystal Structures with the Program Package ToposPro. *Cryst. Growth Des.* **2014**, *14*, 3576−3586.
(46) Bruno, I. J.; Cole, J. C.; Edgington, P. R.; Kessler, M.; Macrae, C. F.; McCabe, P.; Pearson, J.; Taylor, R. New Software for Searching the Cambridge Structural Database and Visualizing Crystal Structures. *Acta Crystallogr., Sect. B: Struct. Sci.* **2002**, *58*, 389−397.
(47) Roztocki, K.; Rauche, M.; Bon, V.; Kaskel, S.; Brunner, E.; Matoga, D. Combining In Situ Techniques (XRD, IR, and 13C NMR) and Gas Adsorption Measurements Reveals CO2-Induced Structural Transitions and High CO2/CH4 Selectivity for a Flexible Metal−Organic Framework JUK-8. *ACS Appl. Mater. Interfaces* **2021**, *13*, 28503−28513.
(48) Shi, Y.-X.; Li, W.-X.; Zhang, W.-H.; Lang, J.-P. Guest-Induced Switchable Breathing Behavior in a Flexible Metal−Organic Framework with Pronounced Negative Gas Pressure. *Inorg. Chem.* **2018**, *57*, 8627−8633.
(49) Cao, Z.; Chen, L.; Li, S.; Yu, M.; Li, Z.; Zhou, K.; Liu, C.; Jiang, F.; Hong, M. A Flexible Two-Fold Interpenetrated Indium MOF Exhibiting Dynamic Response to Gas Adsorption and High-Sensitivity Detection of Nitroaromatic Explosives. *Chem.—Asian J* **2019**, *14*, 3597−3602.
(50) Schwerdtfeger, P.; Nagle, J. K. 2018 Table of Static Dipole Polarizabilities of the Neutral Elements in the Periodic Table. *Mol. Phys.* **2019**, *117*, 1200−1225.
(51) Formalik, F.; Neimark, A. V.; Rogacka, J.; Firlej, L.; Kuchta, B. Pore Opening and Breathing Transitions in Metal-Organic Frameworks: Coupling Adsorption and Deformation. *J. Colloid Interface Sci.* **2020**, *578*, 77−88.
(52) Rogacka, J.; Formalik, F.; Triguero, A. L.; Firlej, L.; Kuchta, B.; Calero, S. Intermediate States Approach for Adsorption Studies in Flexible Metal−Organic Frameworks. *Phys. Chem. Chem. Phys.* **2019**, *21*, 3294−3303.
(53) Hoffman, A. E. J.; Wieme, J.; Rogge, S. M. J.; Vanduyfhuys, L.; Van Speybroeck, V. The Impact of Lattice Vibrations on the Macroscopic Breathing Behavior of MIL-53(Al). *Z. für Kristallogr. -Cryst. Mater.* **2019**, *234*, 529−545.
(54) Evans, J. D.; Bocquet, L.; Coudert, F.-X. Origins of Negative Gas Adsorption. *Chem* **2016**, *1*, 873−886.

https://doi.org/10.1021/acs.chemmater.2c00249
Chem. Mater. XXXX, XXX, XXX−XXX